

A Combined Experimental-Computational Study on the Effect of Topology on Carbon Dioxide Adsorption in Zeolitic Imidazolate Frameworks

William Morris,[†] Ning He,[‡] Keith G. Ray,[§] Peter Klonowski,[†] Hiroyasu Furukawa,[†] Isaak N. Daniels,[‡] Yao A. Houndonougbo,^{||} Mark Asta,[⊥] Omar M. Yaghi,^{†, #, ▽, ○} and Brian B. Laird^{*‡}

[†]Center for Reticular Chemistry, Department of Chemistry and Biochemistry, University of California-Los Angeles, Los Angeles, California, 90095, United States

[‡]Department of Chemistry, University of Kansas, Lawrence, Kansas 66045, United States

[§]Department of Physics, University of California, Berkeley, California 94720, United States

^{||}Department of Chemistry and Biochemistry, Eastern Washington University, Cheney, Washington 99004, United States

[⊥]Department of Materials Science and Engineering, University of California, Berkeley, California 94720, United States

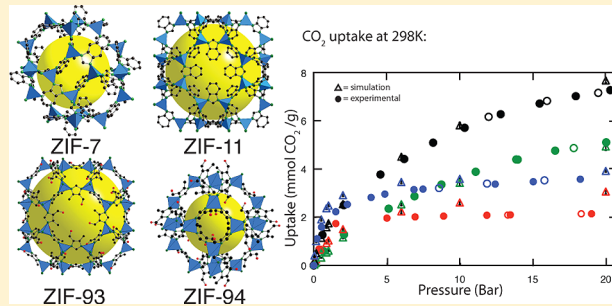
[#]Department of Chemistry, University of California, Berkeley, California 94720, United States

[▽]Molecular Foundry, Division of Materials Sciences, Lawrence Berkeley National Laboratory, Berkeley, California 94720, United States

[○]NanoCentury KAIST Institute and Graduate School of EEWs (WCU), Daejeon 305-701, Korea

S Supporting Information

ABSTRACT: We report CO₂ adsorption data for four zeolitic imidazolate frameworks (ZIFs) to 55 bar, namely ZIF-7, ZIF-11, ZIF-93, and ZIF-94. Modification of synthetic conditions allows access to different topologies with the same metal ion and organic link: ZIF-7 (ZIF-94) having sod topology and ZIF-11 (ZIF-93) having the rho topology. The varying topology, with fixed metal ion and imidazolate functionality, makes these systems ideal for studying the effect of topology on gas adsorption in ZIFs. The experiments show that the topologies with the smaller pores (ZIF-7 and 94) have larger adsorptions than their counterparts (ZIF-11 and 93, respectively) at low pressures (<1 bar); however, the reverse is true at higher pressures where the larger-pore structures have significantly higher adsorption. Molecular modeling and heat of adsorption measurements indicate that while the binding potential wells for the smaller-pore structures are deeper than those of the larger-pore structures, they are relatively narrow and cannot accommodate multiple CO₂ occupancy, in contrast to the much broader potential wells seen in the larger pore structures.



I. INTRODUCTION

Zeolitic imidazolate frameworks (ZIFs) are porous crystalline frameworks comprised of imidazolate and tetrahedral metal ions.¹ ZIFs are a subset of metal–organic frameworks (MOFs) and are of great interest for many gas adsorption applications because, in addition to showing selective gas uptake, they feature high chemical stability, in contrast to many other MOF compounds.² Specifically, ZIFs are materials of interest for applications involving CO₂ separation from flue gas and natural gas sources, which are important in combating global warming and purifying natural gas, respectively.³ Many studies have focused on CO₂ adsorption in ZIFs, both computationally and experimentally.^{4–25} Despite this extensive previous work, the features of a ZIF compound required to obtain high reversible CO₂ adsorption remain incompletely understood.

ZIF compounds can be synthesized with a variety of metal ions, functionalized imidazolate linkers, and with varying topologies.¹ To select ZIFs for CO₂ adsorption applications, it is desirable to understand the role of these several independent variables on gas adsorption, namely, imidazolate functionality, topology, and metal ion. Understanding the role of these structural and chemical variables on gas adsorption in these extended materials is best accomplished by independently varying one variable of interest while keeping others constant in the ZIF framework. Experimental examples of this type of controlled study remain rare, even though a large group of ZIF

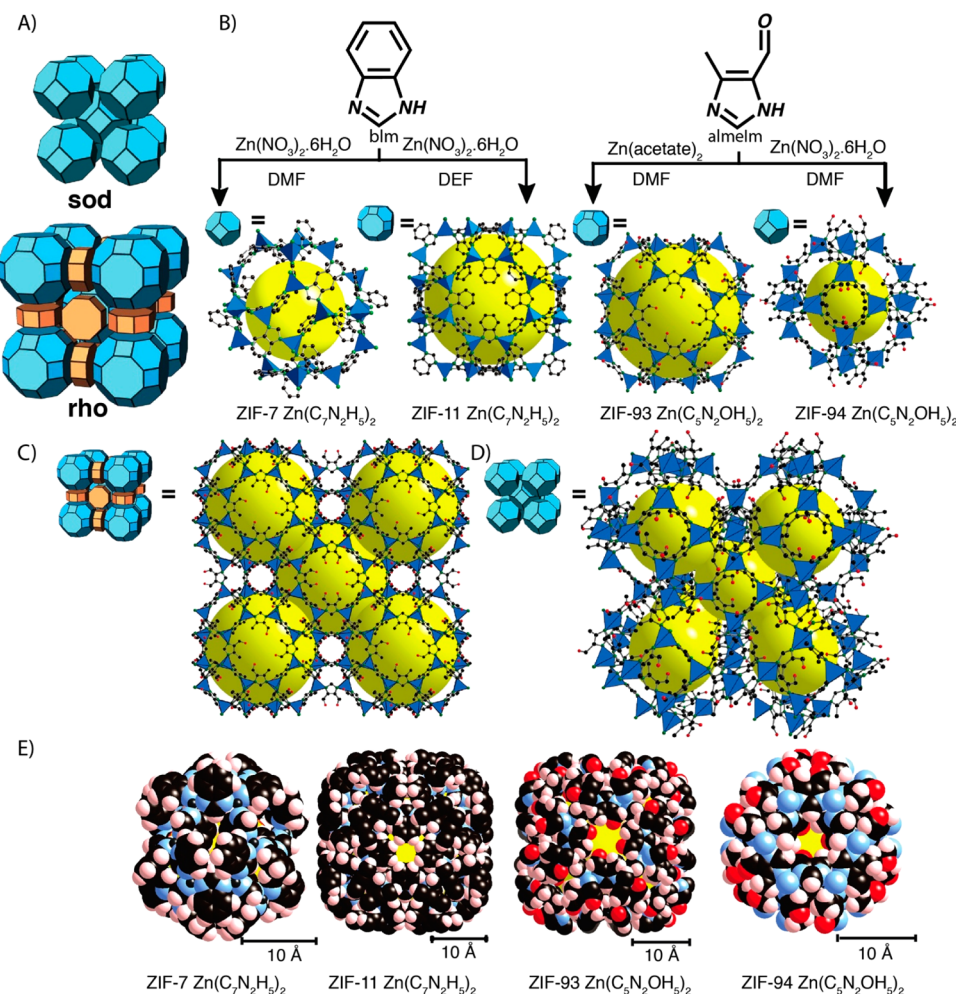
Received: July 19, 2012

Revised: October 11, 2012

Published: October 18, 2012



Scheme 1. (A) The Tiling of the rho and sod Structure Representing the Subdivisions of Space (Blue and Orange Polyhedra);^a (B) Synthesis and Structure of ZIF-7, -11, -93, and -94^b; (C) Packing of Multiple ZIF-93 Unit Cells; (D) Packing of Multiple ZIF-94 Unit Cells. (E) Space Filling Diagrams for ZIF-7, -11, -93, and -94 highlighting the pore apertures, with 10 Å scale bars^c



^aThe **rho** topology consists of two cages: the large **Ita** cage (blue) and the **d8r** cage (orange). ^bThe large **Ita** cages and **sod** cages of the **rho** and **sod** topologies are highlighted. ^cThe yellow ball within the cage represents the free space in the evacuated structure without touching the van der Waals radii of the ZIF atoms. Atom colors: zinc, blue tetrahedral or blue sphere; carbon, black; oxygen, red; nitrogen, green. Hydrogen atoms are omitted for clarity. ZIF-93 and -94 showed in ordered conformation.

frameworks have now been synthesized, encompassing a wide range of functionalized imidazoles and topologies.⁴

Recently, we reported the synthesis of a series of ZIF frameworks with fixed topology (**rho**) in which the imidazolate was decorated with varying functionalities. In this study, we were able to assess the role functionality plays on CO₂ adsorption leading to design principles for significant enhancement of CO₂ adsorption.⁵ Similar work has been performed for a series of **sod** topology ZIFs.²⁶ In the work presented here, we focus on topology and its effect on CO₂ adsorption. We have selected four ZIF frameworks with two topologies, **rho** and **sod** (Scheme 1A), namely ZIF-7, ZIF-11, ZIF-93, and SIM-1 (from here on in ZIF-94) (Scheme 1B–D).^{27B} In each case, a small change in synthetic conditions gives rise to different topologies (Scheme 1B). This synthetic control allows us to synthesize two examples of chemically identical ZIFs with different topologies. First, ZIF-7 and ZIF-11 possess the same metal ion Zn²⁺ and same organic unit benzimidazolate, but different topologies, **sod** and **rho**, respectively (Scheme 1A,B). Second, ZIF-93 and ZIF-94 also exhibit the **rho** and **sod** topology,

respectively, possessing the same metal ion Zn²⁺ and the same organic unit 4-aldemethylimidazolate (Scheme 1A,B).

This level of synthetic control is rare, and it gives us an ideal opportunity to study the role of topology on gas adsorption, which includes effects of pore size and pore aperture (Scheme 1E). Here, we report the first coupled experimental and computational study of the effect of topology on the total CO₂ uptake as a function of pressure, which is one of the principal metrics that must be considered when selecting a framework for CO₂ capture. In addition, we report high-pressure adsorption data for each ZIF. While a number of studies have been made for high-pressure gas adsorption in MOFs,^{28,29} to date the only such study for ZIFs is for ZIF-8. The present study thus provides a unique opportunity to understand the importance of pore metrics when synthesizing ZIFs for gas adsorption applications at high pressure.

II. EXPERIMENTAL METHODS AND RESULTS

Synthesis of each ZIF was adapted from procedures described in the literature (see Experimental Section). For example, ZIF-7

was synthesized by dissolving benzimidazole (3.4 mg, 0.28 mmol) and zinc nitrate hexahydrate (11.4 mg, 3.4 mmol) in 10 mL of *N,N*-dimethylformamide (DMF). The solution was heated at 130 °C for 48 h to form a crystalline powder. Before assessing the porosity and gas adsorption properties of each ZIF, occluded solvent molecules must be removed from the pores. For example, ZIF-7 was first washed with DMF (3×10 mL) over a 2 h period. Second, over a 3 day period, the DMF was replaced with MeOH (3×10 mL). The solvent-exchanged framework was then placed under a vacuum (40 µbar) at 180 °C for 14 h. To confirm the bulk purity of each activated sample, powder X-ray diffraction (PXRD) was performed³⁰ and each ZIF showed analogous structure to the simulated powder pattern.³¹ To further confirm that the solvent was removed from the pores, elemental microanalysis was carried out, the results of which were consistent with calculated formulas.³²

The porosity of ZIF-93 and 94 was evaluated by carrying out N₂ adsorption isotherms at 77 K, which showed a Type I profile indicative of permanent microporosity.³³ Due to the small pore apertures found in ZIF-7 and 11 (Scheme 1C), the N₂ uptake at 77 K showed no meaningful uptake, however, from our adsorption data at 298 K for CO₂, which has a smaller kinetic radius than N₂, it is evident that these materials are porous to molecules of smaller kinetic radii. The surface areas of ZIF-93 and 94 were determined using a Brunauer–Emmett–Teller (BET) analysis of the N₂ isotherms and found to be 864 and 480 m² g⁻¹, respectively. Because of the very low uptake of N₂ at 77 K in ZIF-7 and -11, experimental surface areas were not obtained for these compounds. However, surface areas from simulation were found to be 405(20) m² g⁻¹ and 605(11) m² g⁻¹ for ZIF-7 and -11, respectively. The pore volumes,³⁴ densities, and pore diameters are given in Table 1. The higher density **sod** topologies (7 and 94) have smaller pore volumes and sizes than the lower density **rho** topologies (11 and 93) with larger pore sizes and volumes.

Table 1. Structural Information for ZIF Series

ZIF	composition ^a	topology	density ^a (g cm ⁻³)	pore volume ^{a,b} (cm ³ g ⁻¹)	pore diameter ^a (Å)
-7	Zn(bIm) ₂	sod	1.24	0.207	7.5
-11	Zn(bIm) ₂	rho	1.02	0.457	14.9
-93	Zn(almeIm) ₂	rho	0.99	0.464	17.9
-94	Zn(almeIm) ₂	sod	1.32	0.229	9.1

^aCalculated for solvent-free ZIF. ^bCalculated using PLATON software.³⁴

The CO₂ uptake for each ZIF was first assessed in the low-pressure region below 1.05 bar by analysis of the respective isotherms measured at 298 K, as shown in Figure 1. The filled and open circles show the adsorption and desorption data, respectively. ZIF-94 shows the highest CO₂ uptake in the low-pressure region with an uptake of 2.4 mmol g⁻¹ at 1 bar. Below 1 bar, ZIF-94 with the **sod** topology outperforms its topological counterpart ZIF-93 with the **rho** topology. In addition, between 0.5 and 1 bar, ZIF-7 with the **sod** topology outperforms its counterpart ZIF-11 with the **rho** topology. Because these ZIF pairs have the same imidazolate functionality, this difference can be attributed solely to the differences in topology. Specifically, the adsorption data show that in the low-pressure regime, small pores are advantageous when considering CO₂ adsorption. Interestingly, the isotherms for ZIF-7 show

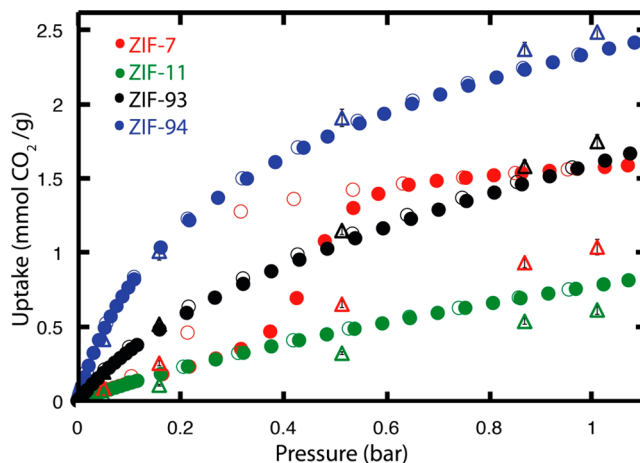


Figure 1. Low-pressure CO₂ isotherms. Experimental (circles) and simulated (triangles) CO₂ isotherms of each ZIF at 298 K: ZIF-7 (red), 11 (green), 93 (black), and 94 (blue). Filled and open circles represent adsorption and desorption branches.

considerable hysteresis, which in previous work has been attributed to a phase transformation, driven by adsorbate-linker interactions and made possible due to the flexibility of the imidazolate link in ZIF-7.^{35,36}

The results at 1 bar can be contrasted with adsorption data obtained at higher pressures, as shown in Figure 2A,B. The CO₂ uptake of ZIF-93 and ZIF-11 exceeds that of ZIF-94 and ZIF-7, respectively. In each case, a crossover pressure between

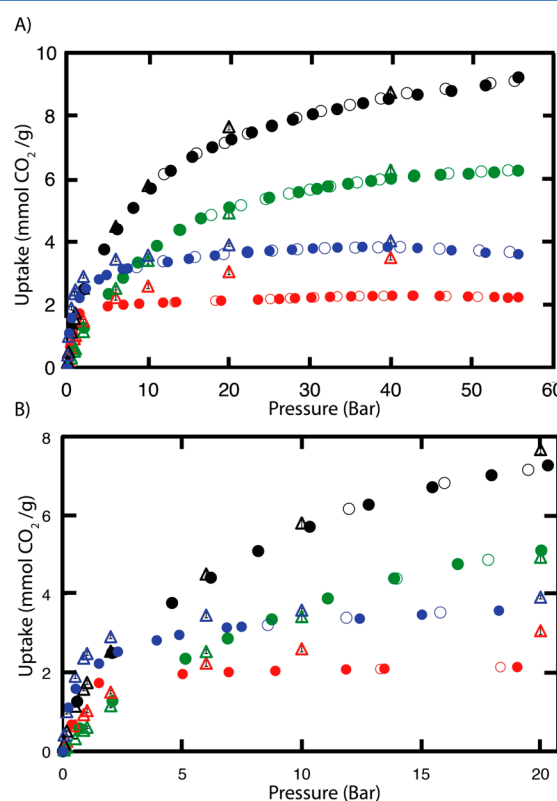


Figure 2. (A) High-pressure CO₂ isotherms to 60 bar. (B) High-pressure CO₂ adsorption to 20 bar. Experimental (circles) and simulated (triangles) CO₂ isotherms of each ZIF at 298 K: ZIF-7 (red), -11 (green), -93 (black), and -94 (blue). Closed and open circles represent adsorption and desorption branches.

2 and 5 bar is observed (see Figure 2B). Below this crossover, the ZIFs with **sod** topology have higher uptakes than their **rho** topology counterparts. Above this crossover, the opposite behavior is observed. The crossover presumably occurs because the smaller pore volumes of ZIF-94 and ZIF-7 saturate at much lower pressures than those of ZIF-93 and ZIF-11.

Isosteric heats of adsorption were calculated from the experimental data for ZIF-11, -93, and -94 by fitting of variable temperature isotherms, as described in the Supporting Information.³⁰ Due to the shape of the isotherm, fitting of experimental adsorption for ZIF-7 was not possible. The isosteric heats of adsorption at infinite dilution, Q_{st}^0 , were found to be 21.6, 29.3, and 30.5 kJ mol⁻¹ for ZIF-11, -93, and -94, respectively. ZIF-94 and ZIF-93 have similar Q_{st}^0 values at infinite dilution, highlighting that the first binding sites for CO₂ are located around their identical organic functionalities. The importance of topology is highlighted by comparing the profile of the Q_{st}^0 , which decreases rapidly in ZIF-93 when compared to ZIF-94. These profiles highlight that the small pores of ZIF-94 offer a stronger binding environment in the low-pressure region when compared to ZIF-93. Interestingly, the Q_{st}^0 for ZIF-93 is 30% higher than that of its topological counterpart ZIF-11, highlighting the importance of functionality.

III. COMPUTATIONAL METHODS AND RESULTS

A. Monte Carlo Modeling of CO₂ Adsorption. In order to obtain a more detailed molecular-level picture of the effect of topology on CO₂ adsorption, we have performed a series of grand canonical Monte Carlo (GCMC) simulations using the program TOWHEE.³⁷ To describe CO₂, we use the three-site Elementary Physical Model 2 (EPM2) of Harris and Young.³⁸ For the van der Waals interactions between the ZIF and CO₂, Lennard-Jones parameters were chosen from the universal force field (UFF)³⁹ and optimized potentials for liquid simulations (OPLS)^{40–42} force field with standard Lorentz–Berthelot mixing rules. Because of the large quadrupole moment of CO₂, charge–charge interactions are important. We obtain atomic partial charges for the various ZIFs by using the REPEAT algorithm^{43–45} to fit the electrostatic potential obtained from periodic density-functional theory using a projector-augmented wave method⁴⁶ and the Perdew–Becke–Ernzerhof generalized gradient approximation,⁴⁷ as implemented in the code VASP.⁴⁸ The values of the charges and other forcefield parameters may be found in the Supporting Information.³⁰

The GCMC results are overlaid in Figures 1 and 2 with open triangles. In the low-pressure range, below one bar, the difference between experiment and simulation is small in ZIF-11 (22%), ZIF-93 (9%), and ZIF-94 (5%) (see Figure 1). At 60 bar, the difference between experiment and simulation is even better in ZIF-11 (4%), ZIF-93 (2%), and ZIF-94 (5%) (see Figure 2A). For ZIF-7, the simulations give reasonable agreement (5–20%) with the experiments in the 5–15 bar range. At higher pressures, significant overestimations (up to 50%) between measurements and simulation results are obtained. At low pressures, there is also significant disagreement; however, this can be largely explained by the fact that a change in structure in the ZIF-7 framework has been observed above a CO₂ pressure of about 0.4 bar from an unknown low-pressure topology to the **sod** topology.²⁷ The authors of ref 27 performed GCMC CO₂ adsorption simulations using the structure seen at the higher pressures, and obtained adsorption values that were significantly overestimated at lower pressure

relative to experimental measurements, but agreed reasonably well around 1 bar, which was the maximum pressure studied. In our simulations of ZIF-7, we also use the high-pressure **sod** structure. Although, our force-field model does not yield as accurate a value in comparison to experiment at 1 bar as does that used in ref 27, our results reproduce well the trends related to the changes in measured adsorptions with changes in topology for both ZIF-7/11 and ZIF-93/94, as well as the quantitative values of the crossover pressures observed experimentally.

An important contribution from the simulations is to determine the preferred adsorption sites and the degree to which they are filled at low and high pressures. To determine the preferential adsorption sites, density maps were calculated for ZIF-93 and -94 at 1.01 and 40 bar (see Figure 3). These

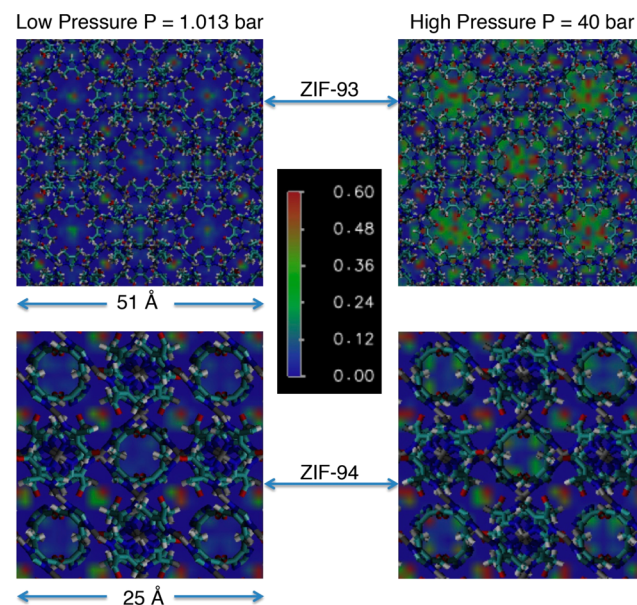


Figure 3. Two-dimensional color-contour adsorbed CO₂ number density maps for ZIF-93 and 94 at low (1.01 bar) and high (40 bar) pressures. The density units are Å⁻³.

maps are two-dimensional contour plots of the number density for the center of mass of CO₂ averaged over the direction normal to the plane of the image. At low pressure, the maps for both ZIF-93 and 94 show that the regions of high adsorbate density are highly localized about the binding sites, that is, singly occupied sites dominate the adsorption at low pressure. At high pressure, there is significant adsorption over a large volume region in ZIF-93, but the adsorption in ZIF-94 is still highly localized around specific binding sites. This indicates that the potential energy wells about the binding sites in ZIF-93 are relatively shallow, allowing the density to spread out significantly at higher pressure, accommodating multiple occupancy. For ZIF-94, the potential wells about the binding sites are deeper than those for ZIF-93 (indicated by the larger adsorption), but are relatively narrow leading to rapid saturation as the pressure is increased. Similar density maps for ZIF-7 and 11 (included in the Supporting Information) show adsorption for **sod** and **rho** topologies that is consistent with those shown for ZIF-93 and 94 in Figure 3.

B. Binding-Energy Analysis. To further elucidate the role of topology in the gas adsorption performance of ZIF-7, -11, -93, and -94, we have analyzed the CO₂ binding energy

landscape for each framework. The results are shown in Figure 4, which plots the binding energy, minimized over 61 CO_2

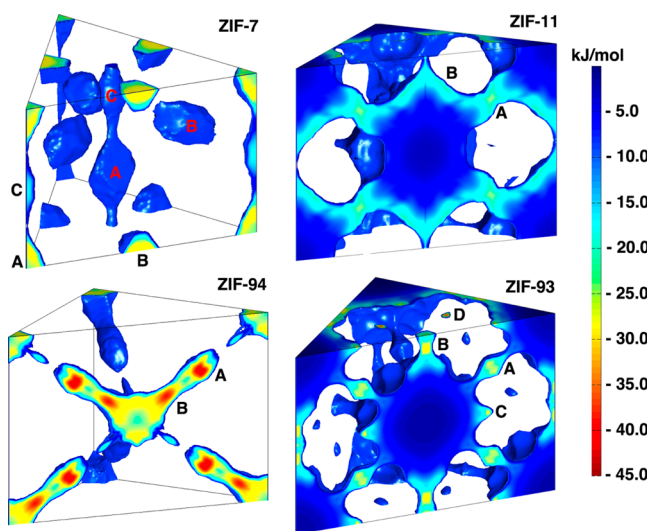


Figure 4. Diagonal $\{110\}$ slices through the cubic unit cells of ZIF-11, -94, and -93, and the rhombohedral unit cell of ZIF-7 showing the binding energy of CO_2 minimized versus orientation and plotted by center of mass position. Important binding regions are indicated by capital letters (A, B, C and D), referred to in the discussion in the text.

orientations, as a function of the CO_2 center of mass position. The binding energies were computed using the Large-scale Atomic/Molecular Massively Parallel Simulator (LAMMPS)⁴⁹ with the same interactions included in the GCMC simulations described above. These results facilitate an analysis of the important binding sites, including the magnitude of the binding energy, the size and shape of the potential-energy wells, and the accessibility of the binding sites.

There are three distinct binding sites in ZIF-7, which we will call A, B, and C. Binding site A, located within a ring of six zinc atoms, has a binding energy of $-29.6 \text{ kJ mol}^{-1}$. Site B, located within a distorted ring of six zinc atoms, has a binding energy of $-31.8 \text{ kJ mol}^{-1}$. Site C, located in the center of the truncated octahedron (Scheme 1) and surrounded by imidazolate linkers, has a binding energy of $-14.3 \text{ kJ mol}^{-1}$. These binding sites are relatively localized compared to the sites found in the **rho** topology ZIFs discussed below. The classical potentials used in this study produce a CO_2 transport barrier from the A site to the C site of roughly 40 kJ mol^{-1} and from the B site to the C site of roughly 52 kJ mol^{-1} . This first barrier represents transport through the vertical channel shown in the center and vertical edges of the ZIF-7 polyhedral section in Figure 4, and the second barrier corresponds to interchannel transport. Transport through the channel is mentioned in previous studies on the “gate-opening” mechanism in ZIF-7.^{35,36}

The primary binding in ZIF-11 occurs in two regions, herein referred to as A and B. The A site is situated within a ring of six zincs and six imidazolate linkers and has a binding energy of $-22.5 \text{ kJ mol}^{-1}$. Binding region B occurs on the inner surface of the largest pore, near the ring of eight zincs at a binding energy of $-27.2 \text{ kJ mol}^{-1}$. This geometry differs from previously reported **rho** ZIFs,⁵ including ZIF-93, described below, where binding occurs within the ring of eight zincs. Both binding regions in ZIF-11 are broad and open onto the large Linde Type A (lta) cavity facilitating multiple occupancies at high pressure. Both binding sites are accessible from this cavity due

to a lack of a high energy barrier. Pore-to-pore transport should be possible through the six-ring channel, passing through site A, with a barrier of roughly 18 kJ mol^{-1} .

Binding in ZIF-94 occurs within a ring of six zincs, which we denote site A, and additionally in the same channel as A, but closer to the center of the pore and surrounded by the functional groups on the linkers, which we denote site B. These sites have binding energies of -40.6 and $-37.8 \text{ kJ mol}^{-1}$ respectively. Binding site A is surrounded by the framework atoms, and binding site B opens to a pore that is relatively small compared with the rho-topology ZIFs. Both these sites are accessible from the pore; however, the CO_2 must pass through the B site to get the A site, which involves a $\sim 15 \text{ kJ mol}^{-1}$ barrier. Between pores, a larger barrier of $\sim 50 \text{ kJ mol}^{-1}$ in one direction and $\sim 37 \text{ kJ mol}^{-1}$ in the other is encountered.

ZIF-93 contains four important binding sites: A, B, C, and D. Site A is within a ring of six zincs, as with ZIF-11. Site B is within the ring of eight zincs, instead of on the surface of the lta cavity as in ZIF-11, most likely due to the smaller functional groups in ZIF-93, which allow CO_2 to fit in this channel. Site C is on the inner surface of the lta cavity in the $\langle 110 \rangle$ direction from the center of this cavity. Site D, represented by ellipsoidal sections in Figure 4, lies between four zincs and four imidazolate linkers and is accessible from site B. The binding energies are -25.3 , -28.0 , -26.6 , and $-37.6 \text{ kJ mol}^{-1}$, respectively. Binding sites A, B, and C open to the large lta cavity. Binding energies in these sites are weaker than in those in ZIF-94, but there is more room for additional CO_2 molecules on the inner surface of the pore. Interpore transport appears possible along the channel through the ring of eight rings as well as the channel through the ring of six zincs.

The binding energy landscapes provide data on the primary binding sites in the four ZIFs considered in this work. The positions and relative strengths of the binding sites identified are consistent with the results given by GCMC density maps described above. CO_2 is more strongly bound in the binding sites found in **sod**-topology ZIF-7 and ZIF-94, relative to those in the corresponding **rho**-topology ZIF-11 and ZIF-93. However, the sites in the **rho** ZIFs open to the large lta cavity with a correspondingly large surface area for additional gas adsorption outside of the deepest wells. Transport barriers determined through classical potentials provide information on binding site accessibility; however, the framework is fixed in these calculations and flexibility in the imidazolate linkers is expected to reduce these barriers.

The trends in the binding energies calculated for the four ZIFs considered in this work can be rationalized as follows, based on an analysis of the electrostatic versus van der Waals contributions to the classical potential models. In ref 5a, it is argued that ZIFs with asymmetrically functionalized imidazolate linkers (that is, having two different functional groups attached to the imidazole ring) tend to produce stronger electrostatic contributions to the CO_2 binding energy. This trend is consistent with the larger average Coulomb contribution to the binding sites in asymmetrically functionalized ZIF-94 ($-10.0 \text{ kJ mol}^{-1}$) compared to ZIF-7 (-6.8 kJ mol^{-1}). However, this is not the case for the **rho** ZIFs considered, because the asymmetrically functionalized ZIF-93 has a smaller average Coulomb contribution, -5.7 kJ mol^{-1} , compared to ZIF-11 (-8.9 kJ mol^{-1}), which suggests that local binding geometry can influence the importance of the electrostatic energy for a particular site. The van der Waals forces favor a large framework surface area close enough to the CO_2 to

maximize the attractive contribution to the Lennard-Jones interactions. This contribution favors the small pores in **sod** ZIF-7 and ZIF-94 when compared to the **rho**-structured ZIF-11 and ZIF-93, which is reflected in the average Lennard-Jones energy, which is -18.9 and $-29.1 \text{ kJ mol}^{-1}$ compared to -15.8 and $-25.0 \text{ kJ mol}^{-1}$, respectively.

IV. CONCLUSIONS

In conclusion, the role of topology on CO_2 adsorption at high and low pressures was investigated in four ZIFs, ZIF-7, -11, -93, and -94 with two topologies, **rho** and **sod**. The importance of topology was highlighted with the small pores of ZIF-7 and ZIF-94 giving rise to higher adsorptions at 1 bar than those obtained for the larger-pore **rho** structures at the same pressure. By contrast, at high-pressure, the adsorption of CO_2 was higher in the large pores of the **rho** structured ZIF-11 and ZIF-93 because of larger pore volumes. Therefore, for each fixed functionality, crossover points were observed where the frameworks with the lower density of large pores (ZIF-11, 93) start to outperform the structures with the higher density of small pores (ZIF-7, -94).

■ EXPERIMENTAL SECTION

Synthesis of ZIF-7, -11, -93, and -94. **ZIF-7.** Zinc nitrate hexahydrate (11.4 mg, 0.381 mmol) and benzimidazole (3.4 mg, 0.28 mmol) were dissolved in 10 mL of DMF in a 20 mL scintillation vial. The vial was heated in an oven at 130°C for 2 days. The crystalline powder was collected by vacuum filtration and washed with DMF ($3 \times 20 \text{ mL}$) over a 1 h period. The ZIF was stored under MeOH, which was exchanged with fresh MeOH ($5 \times 20 \text{ mL}$) over 3 days. The sample was evacuated at 30 mTorr for 12 h 180°C .

ZIF-11. Zinc nitrate hexahydrate (19.4 mg, 0.0652 mmol) and benzimidazole (118 mg, 0.999 mmol) were dissolved in 10 mL of *N,N*-diethylformamide in a 20 mL scintillation vial. The vial was heated in an oven at 130°C for 2 days. The crystalline powder was collected by vacuum filtration and washed with DMF ($3 \times 20 \text{ mL}$) over a 1 h period. The ZIF framework was stored under MeOH, which was exchanged with fresh MeOH ($5 \times 20 \text{ mL}$) over 3 days. The sample was evacuated at 30 mTorr for 12 h 180°C .

ZIF-93. $\text{Zn}(\text{C}_5\text{H}_5\text{N}_2\text{O})_2 = \text{Zn}(\text{almeIm})_2$. A solution of zinc acetate ($\text{Zn}(\text{O}_2\text{CCH}_3)_2$) (0.147 g, 0.8 mmol) in 8 mL of DMF and a solution of 4-methylimidazole-5-carbaldehyde (0.264 g, 2.4 mmol) in 8 mL of DMF was combined and sealed in a 20 mL vial, heated in an oven at 85°C , and allowed to react solvothermally for 12 h. The mother liquor was decanted, and the crystalline powder was washed with chloroform ($3 \times 5 \text{ mL}$). The product was activated with chloroform ($3 \times 10 \text{ mL}$) over 3 days before drying under vacuum (30 mTorr) for 24 h at 80°C . Yield: 0.0191 g, 84% based on 4-methylimidazole-5-carbaldehyde.

ZIF-94. $\text{Zn}(\text{C}_5\text{H}_5\text{N}_2\text{O})_2 = \text{Zn}(\text{almeIm})_2$. A solution of zinc nitrate hexahydrate (0.355 g, 1.37 mmol) in 8 mL of DMF and 4-methylimidazole-5-carbaldehyde (0.6 g, 5.5 mmol) in 10 mL of DMF was combined in a 20 mL scintillation vial and heated in an oven at 85°C , and allowed to react solvothermally for 48 h. The mother liquor was decanted, and the crystalline powder was washed with chloroform ($3 \times 5 \text{ mL}$). The product was activated with chloroform ($3 \times 10 \text{ mL}$) over 3 days before drying under vacuum (30 mTorr) for 24 h at 80°C .

Powder X-ray Diffraction. PXRD data were collected using a Bruker D8-Discover $\theta-\theta$ diffractometer in reflectance Bragg–Brentano geometry employing Ni-filtered Cu $\text{K}\alpha$ line focused radiation at 1600 W (40 kV, 40 mA) power and equipped with a Vantec Line detector. Radiation was focused using parallel focusing Gobel mirrors. The system was also outfitted with an antiscattering shield that prevents incident diffuse radiation from hitting the detector, preventing the normally large background at $2\theta < 3$. Samples were mounted on zero background sample holders by dropping powders from a wide-blade spatula and then leveling the sample with a razor blade. The PXRD data of ZIF-7, -11, -93, and -94 was shown to be consistent with simulated PXRD (see Supporting Information).

Gas Adsorption Measurements. Low-pressure gas adsorption experiments (up to 1.1 bar) were carried out on a Quantachrome Autosorb-1 automatic volumetric gas adsorption analyzer. High-pressure gas adsorption isotherms were measured using the static volumetric method in an HPA-100 from the VTI Corporation (currently Particulate Systems). Ultrahigh-purity grade N₂, He (99.999% purity), and CO₂ gases (99.995% purity) were used in all adsorption measurements.

■ ASSOCIATED CONTENT

Supporting Information

PXRD, N₂ isotherms, and variable temperature gas adsorption. This material is available free of charge via the Internet at <http://pubs.acs.org>.

■ AUTHOR INFORMATION

Corresponding Author

*E-mail: blaird@ku.edu.

Notes

The authors declare no competing financial interest.

■ ACKNOWLEDGMENTS

This material is based upon work supported as part of the Molecularly Engineered Energy Materials, an Energy Frontier Research Center funded by the U.S. Department of Energy, Office of Science, Office of Basic Energy Sciences, under award number DE-SC0001342. This work made use of resources of the National Energy Research Scientific Computing Center, supported by the Office of Science of the U.S. Department of Energy under Contract No. DE-AC02-05CH11231.

■ REFERENCES

- Phan, A.; Doonan, C. J.; Uribe-Romo, F. J.; Knobler, C. B.; O'Keeffe, M.; Yaghi, O. M. *Acc. Chem. Res.* **2010**, *43*, 58–67.
- (a) Banerjee, R.; Furukawa, H.; Britt, D.; Knobler, C.; O'Keeffe, M.; Yaghi, O. M. *J. Am. Chem. Soc.* **2009**, *131*, 3875–3877. (b) Wang, B.; Côté, A. P.; Furukawa, H.; O'Keeffe, M.; Yaghi, O. M. *Nature* **2008**, *453*, 207–211. (c) Park, K. S.; Ni, Z.; Côté, A. P.; Choi, J. Y.; Huang, R.; Uribe-Romo, F. J.; Chae, H. K.; O'Keeffe, M.; Yaghi, O. M. *Proc. Natl. Acad. Sci. U.S.A.* **2006**, *103*, 10186–10191.
- (3) (a) Li, J.-R.; Ma, Y.-G.; McCarthy, M.; Sculley, J.; Yu, J.-M.; Jeong, H.-K.; Balbuena, P. B.; Zhou, H.-C. *Chem. Rev.* **2011**, *111*, 1791–1823. (b) Sumida, K.; Rogow, D. L.; Mason, J. A.; McDonald, T. M.; Bloch, E. D.; Herm, Z. R.; Bae, T.-H.; Long, J. R. *Chem. Rev.* **2012**, *112*, 724–781.
- (4) (a) Banerjee, R.; Phan, A.; Wang, B.; Knobler, C.; Furukawa, H.; O'Keeffe, M.; Yaghi, O. M. *Science* **2008**, *319*, 939–943.
- (5) (a) Morris, W.; Leung, B.; Furukawa, H.; Yaghi, O. K.; He, N.; Hayashi, H.; Hounoungbo, Y.; Asta, M.; Laird, B. B.; Yaghi, O. M. *J. Am. Chem. Soc.* **2010**, *132*, 11006–11008. (b) Ray, K. G.; Olmsted, D.;

- He, N.; Houndoungbo, Y.; Laird, B. B.; Asta, M. *Phys. Rev. B* **2012**, *85*, 085410.
- (6) Perez-Pellitero, J.; Amrouche, H.; Siperstein, F. R.; Pirngruber, G.; Nieto-Draghi, C.; Chaplais, G.; Simon-Masseron, A.; Bazer-Bachi, D.; Peralta, D.; Bats, N. *Chem.—Eur. J.* **2010**, *16*, 1560–1571.
- (7) Battisti, A.; Taioli, S.; Garberoglio, G. *Microporous Mesoporous Mater.* **2011**, *143*, 46–53.
- (8) Rankin, R. B.; Liu, J.; Kulkarni, A. D.; Johnson, J. K. *J. Phys. Chem. C* **2009**, *113*, 16906–16914.
- (9) Liu, J.; Keskin, S.; Sholl, D. S.; Johnson, J. K. *J. Phys. Chem. C* **2011**, *115*, 12560–12566.
- (10) Sirjoossingh, A.; Alavi, S.; Woo, T. K. *J. Phys. Chem. C* **2010**, *114*, 2171–2178.
- (11) Keskin, S.; Liu, J.; Rankin, R. B.; Johnson, J. K.; Sholl, D. S. *Ind. Eng. Chem. Res.* **2009**, *48*, 2355–2371.
- (12) Getman, R. B.; Bae, Y.-S.; Wilmer, C. E.; Snurr, R. Q. *Chem. Rev.* **2012**, *112*, 703–723.
- (13) Huang, H.; Zhang, W.; Liu, D.; Liu, B.; Chen, G.; Zhong, C. *Chem. Eng. Sci.* **2011**, *66*, 6297–6305.
- (14) Bux, H.; Chmelik, C.; van Baten, J. M.; Krishna, R.; Caro, J. *Adv. Mater.* **2010**, *22*, 4741–4743.
- (15) Hou, X.-J.; Li, H. *J. Phys. Chem. C* **2010**, *114*, 13501–13508.
- (16) Li, B.; Wei, S.; Chen, L. *Mol. Simul.* **2011**, *37*, 1131–1142.
- (17) Liu, D.; Zheng, C.; Yang, Q.; Zhong, C. *J. Phys. Chem. C* **2009**, *113*, 5004–5009.
- (18) Babarao, R.; Dai, S.; Jiang, D. *J. Phys. Chem. C* **2011**, *115*, 8126–8135.
- (19) Wells, B. A.; Chaffee, A. L. *Adsorption* **2011**, *17*, 255–264.
- (20) Wilmer, C. E.; Snurr, R. Q. *Chem. Eng. J.* **2011**, *171* (3), 775–781.
- (21) Atci, E.; Keskin, S. *Ind. Eng. Chem. Res.* **2012**, *51*, 3091–3100.
- (22) Thornton, A. W.; Dubbeldam, D.; Liu, M. S.; Ladewig, B. P.; Hill, A. J.; Hill, M. R. *Energy Environ. Sci.* **2012**, *5*, 7637–7646.
- (23) Poloni, R.; Smit, B.; Neaton, J. B. *J. Phys. Chem. A* **2012**, *116*, 4957–4964.
- (24) McDaniel, J. G.; Yu, K.; Schmidt, J. R. *J. Phys. Chem. C* **2012**, *116*, 1892–1903.
- (25) Chen, E.-Y.; Liu, Y.-C.; Zhou, M.; Zhang, L.; Wang, Q. *Chem. Eng. Sci.* **2012**, *71* (26), 178–184.
- (26) Amrouche, H.; Aguado, S.; Perez-Pellitero, J.; Chizallet, C.; Siperstein, F.; Farrusseng, D.; Bats, N.; Nieto-Draghi, C. *J. Phys. Chem. C* **2011**, *115*, 16425–16432.
- (27) Aguado, S.; Nicolas, C.; Moizan-Baslé, V.; Nieto, C.; Amrouche, H.; Bats, N.; Audebrand, N.; Farrusseng, D. *New J. Chem.* **2011**, *35*, 41–44. (b) Aguado, S.; Canivet, J.; Farrusseng, D. *Chem. Commun.* **2010**, *46*, 7999–8001.
- (28) Llewellyn, P. L.; Bourrelly, S.; Serre, C.; Vimont, A.; Daturi, M.; Hamon, L.; Weireld, G. D.; Chang, J.-S.; Hong, D.-Y.; Hwang, Y. K.; et al. *Langmuir* **2008**, *24*, 7245–7250.
- (29) Furukawa, H.; Ko, N.; Go, Y. B.; Aratani, N.; Choi, S. B.; Choi, E.; Yazaydin, A. O.; Snurr, R. Q.; O'Keeffe, M.; Kim, J.; et al. *Science* **2010**, *239*, 424–428.
- (30) See Supporting Information for full experimental data including synthetic conditions, PXRD, and additional simulation data.
- (31) Nune, S. K.; Thallapally, P. K.; Dohnalkova, A.; Wang, C.; Liuc, J.; Exarhos, G. J. *Chem. Commun.* **2010**, *46*, 4878–4880.
- (32) Elemental microanalysis percentages for activated samples (in parentheses calculated values): ZIF-7 Zn(bIm)₂: C 55.71(56.12); H 3.41(3.36); N 18.87(18.70), ZIF-11 Zn(bIm)₂: C 55.74(56.12); H 3.21(3.36); N 19.14(18.70), ZIF-93 Zn(mealIm)₂: C 42.01 (42.35); H 3.60(3.55); N 19.64(19.79), ZIF-94 Zn(mealIm)₂: C 42.15(42.35); H 3.49(3.55); N 19.80(19.79).
- (33) Roswell, J. L. C.; Yaghi, O. M. *J. Am. Chem. Soc.* **2006**, *128*, 1304–1315.
- (34) Spek, A. L. *J. Appl. Crystallogr.* **2003**, *36*, 7–13.
- (35) Aguado, S.; Bergeret, G.; Titus, M. P.; Moizan, V.; Nieto-Draghi, C.; Bats, N.; Farrusseng, D. *New J. Chem.* **2011**, *35*, 546–550.
- (36) Gucuyener, C.; van den Bergh, J.; Gascon, J.; Kapteijn, F. *J. Am. Chem. Soc.* **2010**, *132*, 17704–17706.
- (37) Martin, G. M.; Siepmann, J. I. *J. Phys. Chem. B* **1999**, *103*, 4508–4517.
- (38) Harris, J.; Yung, K. *J. Phys. Chem.* **1995**, *99*, 12021–12024.
- (39) Rappe, A. K.; Casewit, C. J.; Colwell, K. S.; Goddard, W. A., III; Skiff, W. M. *J. Am. Chem. Soc.* **1992**, *114*, 10024–10035.
- (40) Rizzo, R. C.; Jorgensen, W. L. *J. Am. Chem. Soc.* **1999**, *121*, 4827–4836.
- (41) Jorgensen, W. L.; Maxwell, D. S.; Tirado-Rives, J. *J. Am. Chem. Soc.* **1996**, *118*, 11225–11236.
- (42) Jorgensen, W. L.; Madura, J. D.; Swenson, C. J. *J. Am. Chem. Soc.* **1984**, *106*, 6638.
- (43) Campaña, C.; Mussard, B.; Woo, T. K. *J. Chem. Theory Comput.* **2009**, *5*, 2866–2878.
- (44) Vaidyanathan, R.; Iremonger, S. S.; Shimizu, G. K. H.; Boyd, P. G.; Alavi, S.; Woo, T. K. *Science* **2010**, *330*, 650–653.
- (45) Vaidyanathan, R.; Iremonger, S. S.; Shimizu, G. K. H.; Boyd, P. G.; Alavi, S.; Woo, T. K. *Angew. Chem.* **2012**, *51*, 1826–1829.
- (46) Blöchl, P. *Phys. Rev. B* **1994**, *50*, 17953–17979.
- (47) Perdew, J. P.; Burke, K.; Ernzerhof, M. *Phys. Rev. Lett.* **1996**, *77*, 3865–3868.
- (48) Kresse, G.; Furthmüller, J. *J. Phys. Rev. B* **1996**, *54*, 11169–11186. (b) Kresse, G.; Joubert, D. *Phys. Rev. B* **1999**, *59*, 1758–1775.
- (49) Plimpton, S. *J. Comput. Phys.* **1995**, *117*, 1–19.